INTERNATIONAL JOURNAL OF HYDROGEN ENERGY 45 (2020) 7339–7353

Available online at www.sciencedirect.com

ScienceDirect

journal homepage: www.elsevier.com/locate/he

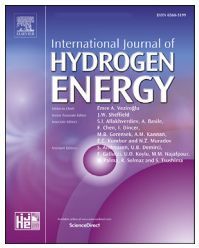

Multi-scale model based design of membrane reactor/separator processes for intensified hydrogen production through the water gas shift reaction

Seçgin Karagöz [a], Theodore T. Tsotsis [b], Vasilios I. Manousiouthakis [a,*]

[a] Department of Chemical Engineering, Bursa Technical University, Mimar Sinan Campus, 16310, Bursa, Turkey
[b] Mork Family Department of Chemical Engineering & Materials Science, University of Southern California, Los Angeles, Los Angeles, CA, 90089, USA

HIGHLIGHTS

- Dusty Gas Model comparison with other diffusion flux models, in membrane reactors.
- Multi-scale model simulation based process design.
- Membrane-Separator/Membrane-Reactor based WGSR intensifying designs.

ARTICLE INFO

Article history:
Received 21 February 2019
Received in revised form
16 April 2019
Accepted 14 May 2019
Available online 12 February 2020

Keywords:
Membrane
Reactor
Dusty-Gas
Multiscale
Water gas shift reaction (WGSR)

ABSTRACT

This work aims to first quantify the impact of various diffusion models (Maxwell-Stefan, Wilke, Dusty-Gas) on the predictions of a multi-scale membrane reactor/separator mathematical model, and to then demonstrate this model's use for the design and process intensification of membrane reactor/separator systems for hydrogen production. This multi-scale model captures velocity, temperature and species' concentration profiles along the catalyst pellet's radial direction, and along the reactor's axial direction, by solving the momentum, energy, and species transport equations, accounting for convection, conduction, reaction, and diffusion mechanisms. In the first part of work, the effect of pellet-scale design parameters (mean pore diameter, volumetric porosity, tortuosity factor, etc.) and various species' flux models on the model predictions is studied. In the second part, the study focuses on the comparison, in terms of their process intensification characteristics, of various hydrogen production processes. These include a conventional high-temperature shift reactor (HTSR)/low-temperature shift reactor (LTSR) sequence, a novel HTSR/membrane separator (MS)/LTSR/MS sequence, and a process that involves low-temperature shift membrane reactors-LTSMR in a series.

© 2019 Hydrogen Energy Publications LLC. Published by Elsevier Ltd. All rights reserved.

* *Corresponding author.*
E-mail address: vasilios@ucla.edu (V.I. Manousiouthakis).
https://doi.org/10.1016/j.ijhydene.2019.05.118
0360-3199/© 2019 Hydrogen Energy Publications LLC. Published by Elsevier Ltd. All rights reserved.

Introduction

Efforts for the development of more efficient hydrogen production technologies have been gaining momentum, for both mobile and stationary applications [1], due to the worldwide drive for more green processes, the prospects of hydrogen as an important energy carrier, and its current industrial uses [2]. Indeed, hydrogen has the potential to become the leading actor in energy [3], especially given its importance for fuel cell based vehicular transportation [4], and clean power generation [5].

Hydrogen can be generated from both nonrenewable and renewable energy sources. It is commercially manufactured from natural gas, liquid hydrocarbons, coal and biomass [6], with natural gas being the leading hydrogen source [7]. Production efficiency largely determines which energy source is used for hydrogen production, and therefore, prominent increases in the efficiency of hydrogen production processes can play an important role in accelerating the onset of the hydrogen economy [8].

The heterogeneously catalyzed Water Gas Shift Reaction (WGSR) is an industrially important, integrated chemical process [8], with increasing number of applications for fuel cell grade hydrogen [9], and PEM fuel cells [10]. WGSR kinetics have been discussed at low temperatures [11], both high and low temperatures [12], and in membrane reactor settings [13]. WGSR kinetics have been comprehensively reviewed in [14], and multiple aspects of WGSR have been reviewed in [15].

Reactor-scale level modeling of the WGSR has been carried out for Pd-based membrane reactors [16], and, in two dimensions, for packed bed [5], and co-current/counter-current membrane reactors [17], while more recently the performance of the WGSR in membrane reactors has been assessed using reactor-scale level, two dimensional, modeling [18], and artificial neural network approaches, [19].

According to the literature, the set of basic features for the WGSR are:

(1) the WGSR reaction is expressed as:

$$CO + H_2O \Leftrightarrow CO_2 + H_2 \quad \left(\Delta H^0_{298K} = -41.1 kJ/mol\right) \tag{1}$$

(2) The WGSR is moderately exothermic, reversible and equilibrium limited in nature, (3) the desired level of carbon monoxide (CO) reduction occurs at low temperatures with favorable kinetics at higher temperatures, (4) The WGSR tends to shift towards the reactants' side at high temperatures, (5) the equilibrium conversion of CO is independent of the pressure because of no variation in the number of moles while the reaction occurs, (6) the equilibrium conversion of CO is only a function of temperature and feed composition [12,14,15].

The reactor, separator, reactor-separator mathematical model employed in this work, is multi-scale in nature, has been derived through repeated application of the Reynolds Transport Theorem (RTT), and has recently been put forward by our group to capture the performance of reactors [20], membrane reactors [21], and membrane reactors/adsorptive reactors [22]. In this work, the aforementioned multiscale model is experimentally validated; is applied to reactors, membrane separators, and membrane reactors; is employed in evaluating the performance of several novel intensifying membrane reactor/separator designs for the Water Gas Shift Reaction; and is used to carry out a comparative evaluation of the impact of various diffusion models (Maxwell-Stefan, Wilke, Dusty-Gas). In most literature studies, simplified diffusion models are employed, as well as assumptions of uniform temperature and pressure gradients throughout the spherical pellet. In this work, several diffusion models (including the rigorous Dusty Gas Model) are comparatively evaluated, and the above uniformity assumptions are overcome. Subsequently, the effect of design parameters at the pellet-scale (mean pore diameter, volumetric porosity, tortuosity factor, etc.) and reactor-scale (inlet gas temperature, inlet H_2O/CO ratio of 5, etc.) on process performance is studied. Especially, it is demonstrated that the catalyst effectiveness factor exhibits significant axial variation along the reactor length for the aforementioned diffusion flux models. Finally, the resulting multiscale model is used to develop practical insights into the performance of various WGSR system configurations, as process design and intensification studies are carried out for WGSR based hydrogen production. The performance of various WGSR process designs is evaluated, including the conventional high temperature shift reactor-HTSR/low temperature shift reactor-LTSR sequence, and the two novel sequences proposed in this work, consisting of HTSR/MS/LTSR/MS, and LTMR-LTMR systems in series. These sequential, flexible, multi-component syngas clean-up/reaction/separation multi-product systems hold the promise of minimizing capital and operating costs, and maximizing the profitability of IGCC power plants by increasing their power generation capacity.

Intensified reactor-separator designs for hydrogen-based power generation

A conventional Integrated Gasification Combined Cycle (IGCC) power generation plant converts coal into syngas (containing $CO/H_2/CO_2$ with small amounts of CH_4 and impurities) via a high-pressure gasifier in the presence of steam and oxygen. An abstraction of this process is illustrated in Fig. 1, which can also emulate a hydrogen production plant converting natural gas into syngas via a high pressure reformer (rather than gasifier) in the presence of steam. In industry, the gas stream entering the water gas shift reactor section typically goes through a high-temperature shift reactor (HTSR) operating in the range of 300 °C–450 °C and utilizing Fe_3O_4 –Cr_2O_3–CuO based catalysts, an intercooler, and a low-temperature shift reactor (LTSR) operating in the range of 200 °C–300 °C and utilizing Cu–ZnO–Al_2O_3 based catalysts, [12,21,22]. Reaction equilibrium is nearly attained at the exit of this combined HTSR + Cooler + LTSR system, which through the use of excess steam ensures near complete CO conversion.

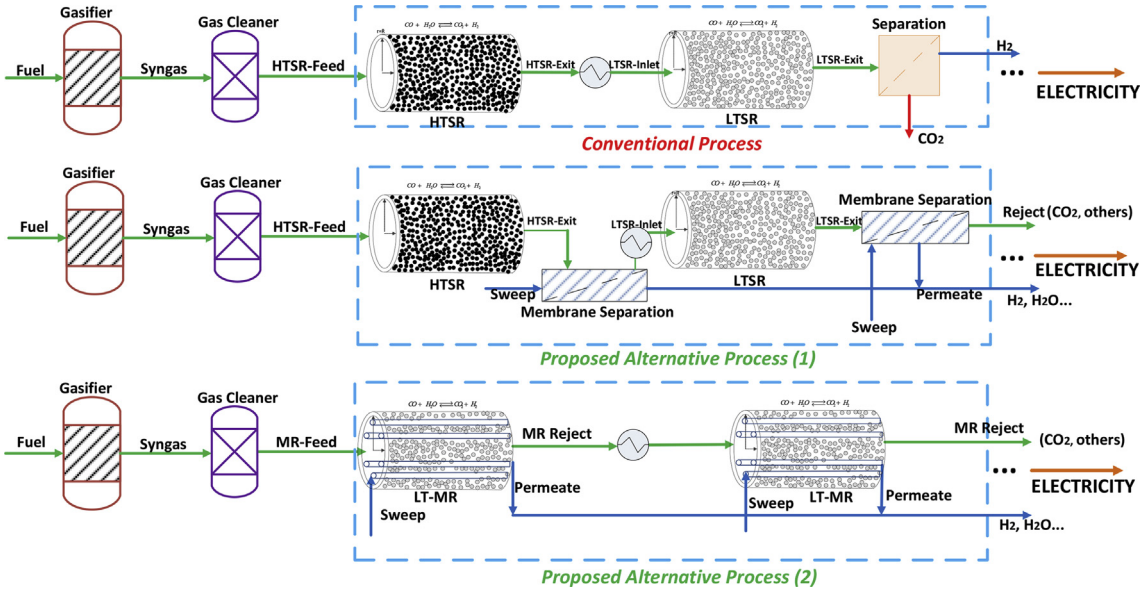

Fig. 1 – Conceptual representation of considered hydrogen-based power generation design alternatives.

In this work, two intensified reactor-separator design alternatives are considered to the above conventional hydrogen-based power generation process. The first design alternative incorporates membrane separator (MS) units and consists of an HTSR/MS/LTSR/MS sequence. The second design alternative consists of a sequence of two low-temperature membrane reactors (LTMR), with an intermediate cooler. Integrating reaction and separation in carrying out the WGSR is a well-suited process intensification concept, as it holds the potential to improve efficiency and economics, through decreased operating temperatures, higher CO conversion levels, and reduced capital costs associated with lower catalyst use and lower downstream separation loads.

Comparative evaluation of alternative pellet scale diffusion models

The employed reactor, separator, reactor-separator, multi-scale, mathematical model [20–22], considers two scale levels (see Fig. 2): the micro (pellet) scale considers such features as, pellet size, average pore size, reaction kinetic rates, pellet material properties, and pellet shape, while the macro (reactor) scale considers such features as reactor tube dimensions, catalyst packing void fraction, and others. In particular, the HTSRs and LTSRs are composed of the catalyst pellet domain and the reactor domain (bulk gas phase), the MSs of the separator domain (bulk gas phase) and the permeation domain, while the MRs consist of the catalyst pellet domain, the reactor domain (bulk gas phase) and the permeation domain.

Numerical computations of the transport equations at the pellet and reactor scales are carried out interactively. The information exchanged among the domains includes gas pressure, temperature, velocity, and species' concentrations. Some exchanged information is often formalized in the form of species' effectiveness factors.

The resulting equations are implemented in the COMSOL Multiphysics® Version 5.0 software package and solved simultaneously in all aforementioned domains along the length of the LTSR, HTSR, MS, and MR, using the finite

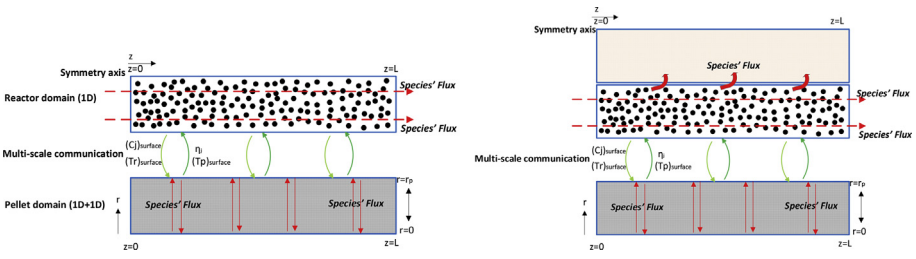

Fig. 2 – Multi-scale reactor scheme, packed bed reactor (left), membrane reactor (right).

element method (FEM). The computational fluid dynamics model employs a uniform (fine) mesh in the reactor domain, and a non-uniform mesh with 8000-unit cells in the catalyst pellet domains. For the radial direction of both catalyst pellets, we use a pre-defined mesh element distribution available in the COMSOL software, which maintains the above total number of elements in the radial direction, while ensuring that smaller unit cells are employed near the pellet surface. Halving of the mesh size did not yield any noticeable changes in the obtained results. In order to gauge the impact of the underlying transport and reaction (catalyst pellet) process, instantaneous effectiveness factors are calculated. They are defined as ratios of the real uptake rate (due to combined transport and reaction or adsorption) of a given species by the catalyst/adsorbent pellet over the same uptake rate in the absence of transport limitations, i.e., when the gas phase concentration within the particle is the same with that prevailing at the pellet's external surface. The effectiveness factor for the ith species is defined by Eq. (3), the superscript refering to either the catalyst or the adsorbent pellet. For the catalyst pellet, the effectiveness factors of all species are equal, since there is only one reaction (WGSR) taking place in the pellet with equal stoichiometric coefficients for all species.

$$\eta_i^{\zeta} \widehat{=} \frac{\iint_{CS}\left(\varepsilon_{f,A}^{\zeta}\overrightarrow{N_i^{\zeta}}\right)\cdot\vec{n}\,dA^t}{\iiint_{CV} M_i\varepsilon_{s,V}^{\zeta}\rho_{c/a}\overrightarrow{R_i^{\zeta}}|_{CS}dV} = \frac{\text{the net mass flow of ith species at pellet's surface}}{\text{the volumetric mass generation rate of the same species}}; i = 1,\upsilon \tag{3}$$

Most industrially relevant reactions take place in multiphase reactors such as packed bed, moving bed, trickle bed, two and three-phase fluidized beds, bubble columns, and stirred tanks [21,24,25]. Traditional packed bed reactor models can be either pseudo-homogeneous, or heterogeneous [26], with the latter enabling an enhanced level of accuracy [27]. In these reactor types, catalyst pellets are often employed, within which simultaneous, multicomponent reaction and transport occurs that must be properly modeled [28]. This detailed level of modeling, where transport equations are solved in each phase, can account for gradients inside each phase and across, and thus provide enhanced fidelity in the model predictions [29]. Such enhanced fidelity can play an important role in accelerating the scale-up process, from the laboratory to the industrial scales, by allowing for example the spatial variation of catalyst pellet effectiveness factors, as the use of larger size pellets may be necessary in commercial reactors, to avoid large pressure drops. In fact, due to the high exothermicity of the WGSR, heat management is a key design consideration and constraint for both traditional packed-bed and MR reactors, particularly for the high-pressure IGCC conditions of interest in this study.

The goal of this work, therefore, is the development of a multi-scale MR model, which captures in detail the species/energy transport phenomena within the porous catalyst pellets, and their dependence on the pellet's spatial location in the reactor, as well as the species/energy transport phenomena in the reactor's bulk gas phase. Throughout this work, catalyst pellet effectiveness factors are calculated for various pellet sizes. The derivation of the MR model equations was demonstrated and discussed in earlier publications [20,21], and is also directly applicable to the HTSR, LTSR, and MS units employed in this work.

Dusty gas model (DGM)

In most industrial packed bed reactors, the reactions carried out involve more than two species. Thus, advanced multicomponent flux models, such as the Dusty Gas Model (DGM), are required to capture species transport within catalyst pellets. Quantification of the combined diffusion-convection mass flux $\overrightarrow{N_{\gamma,i}^{\alpha}}$ of species i within the pellet domain is carried out using the DGM, which takes into account three species' transport mechanisms: continuum (or regular) diffusion described by the Maxwell-Stefan equations, viscous diffusion (or convection), and Knudsen diffusion. Continuum diffusion is the movement of species due to concentration gradients, viscous diffusion is the movement of species due to pressure gradients, and Knudsen diffusion is the movement of species due to concentration gradients in the presence of small pore walls. Thermal diffusion is not considered in this work. The resulting DGM constitutive equations, relating the combined (convective and diffusive) molar fluxes in systems with walls, with the underlying species' concentration gradients, are:

$$-\frac{1}{\sum_{j=1}^{N_s} c_j}\sum_{\substack{j=1\\ j\neq i,p}}^{N_s}\left(\frac{c_j}{D_{ij}^{eff}}\overrightarrow{N_i} - \frac{c_j}{D_{ij}^{eff}}\overrightarrow{N_j}\right) - \frac{\overrightarrow{N_i}}{D_{iK}^{eff}} = \vec{\nabla}c_i + \frac{c_i}{\sum_{i=1}^{N_s} c_i RT}\left(1 + \frac{P^p}{D_{iK}^{eff}}\frac{B_O}{\mu_f^{\alpha}}\right)\vec{\nabla}P^p; i = 1, N_s \tag{4}$$

The combined molar fluxes $\overrightarrow{N_i}$, combined mass fluxes $\overrightarrow{J_i}$, and velocities $\overrightarrow{v_i}$ for the ith species, are defined as $\overrightarrow{N_i} = c_i\overrightarrow{v_i}$, $\overrightarrow{J_i} = M_i c_i \overrightarrow{v_i}$.

The DGM can be written in matrix equation form for the N_s species as follows:

$$\begin{bmatrix} \overrightarrow{N_1} \\ \vdots \\ \overrightarrow{N_j} \end{bmatrix} = - \underbrace{\begin{bmatrix} \left(\frac{\sum_{i=2}^{Ns} \frac{c_i}{D_{1i}^{eff}}}{\sum_{j=1}^{Ns} c_j} + \frac{1}{D_{1K}^{eff}}\right) & \frac{-c_1}{D_{12}^{eff} \sum_{j=1}^{Ns} c_j} & \cdots & \frac{-c_1}{D_{1j}^{eff} \sum_{j=1}^{Ns} c_j} \\ \frac{-c_2}{D_{21}^{eff} \sum_{j=1}^{Ns} c_j} & \left(\frac{\sum_{i=1, i\neq 2}^{Ns} \frac{c_i}{D_{2i}^{eff}}}{\sum_{j=1}^{Ns} c_j} + \frac{1}{D_{2K}^{eff}}\right) & \cdots & \frac{-c_2}{D_{2j}^{eff} \sum_{j=1}^{Ns} c_j} \\ \vdots & \vdots & \ddots & \vdots \\ \frac{-c_j}{D_{j1}^{eff} \sum_{j=1}^{Ns} c_j} & \frac{-c_j}{D_{j2}^{eff} \sum_{j=1}^{Ns} c_j} & \cdots & \left(\frac{\sum_{i=1, i\neq j}^{Ns} \frac{c_i}{D_{ji}^{eff}}}{\sum_{j=1}^{Ns} c_j} + \frac{1}{D_{jK}^{eff}}\right) \end{bmatrix}^{-1}}_{D^{DGM}} \cdot \underbrace{\begin{bmatrix} \overrightarrow{\nabla} c_1 + \frac{c_1}{\sum_{j=1}^{N_s} c_j RT} \left(1 + \frac{P}{D_{1K}^{eff}} \frac{B_O}{\mu_f}\right) \overrightarrow{\nabla} P \\ \vdots \\ \overrightarrow{\nabla} c_j + \frac{c_j}{\sum_{j=1}^{N_s} c_j RT} \left(1 + \frac{P}{D_{jK}^{eff}} \frac{B_O}{\mu_f}\right) \overrightarrow{\nabla} P \end{bmatrix}}_{\overrightarrow{\nabla} \Omega}$$

Then a DGM effective diffusivity matrix can be defined as D^{DGM} and give rise to the equation

$$\overrightarrow{N} = - D^{DGM} \cdot \overrightarrow{\nabla} \Omega \tag{5}$$

Maxwell-Stefan Model (MSM) and Wilke Model (WM)

Alternative to DGM, the diffusive fluxes, in the catalyst-pellet domain, can also be calculated using the Maxwell-Stefan Model (MSM) and the Wilke Model (WM). In the literature, multicomponent diffusivities are defined in two frameworks (the generalized Fick's- and Maxwell-Stefan equations) by several alternative models. The bulk diffusion flux models considered are the Fick's first law for binary mixtures, the approximate Fickian Wilky model, the generalized Fick's first law, and the rigorous Maxwell-Stefan model. On the other hand, the Fickian Wilke-Bosanquet and dusty gas models are considered for the combined bulk and Knudsen diffusion fluxes. The dusty gas model is the extended form of the Maxwell-Stefan model for porous media transport [24].

The MSM equation is given in the following form:

$$\overrightarrow{\nabla} x_i = \sum_{j=1}^{N_s} \frac{x_i x_j}{D_{ij}^{eff}} \left(\frac{1}{\rho_j} \overrightarrow{j_j} - \frac{1}{\rho_i} \overrightarrow{j_i}\right) + (w_i - x_i) \left(\frac{\overrightarrow{\nabla} P}{P}\right) \tag{6}$$

The WM equation is given in the following form:

$$\overrightarrow{j_i} = - D_{im} \overrightarrow{\nabla} \rho_i, \; where \; D_{im} = \frac{1 - w_i}{M \sum_{\substack{j=1 \\ j\neq i}}^{N_s} \frac{w_j}{M_j D_{ij}}} \tag{7}$$

The kinetics of the WGS reaction have been described in a multitude of literature studies, using different rate expressions and mechanisms (Langmuir-Hinshelwood, Redox and empirical – Power-law). Empirical-power-law rate expressions are typically preferred by most researchers [30,31]. In this study, a commercial Co–Mo/Al2O3 catalyst is selected for the LTSR, and a commercial Fe2O3–Cr2O3 catalyst is selected for the HTSR in this study. The associated empirical-power-law WGSR kinetic rate expressions and parameters are obtained based on experimental results. They incorporate an Arrhenius Law expression to account for the kinetic rate's temperature dependence and are listed in Table 1.

In this study, the reactor and pellet domain property dependencies are shown in Table 2.

The effect of these diffusion models (DGM, MSM, WM) on the predictions of the employed multi-scale reactor/separator mathematical model is discussed in the results section.

Results and discussion

Alternative diffusion model results

Experimental model validation

In our lab-scale experimental investigations of the WGSR, we utilized a commercial Co–Mo/Al_2O_3 shift catalyst that has been shown to exhibit high activity and stability for the low-temperature shift process. The relevant WGSR parameters are shown in Table 3. We used the developed multi-scale

Table 1 – Chemical model equations.

LTSR Reaction Rate: $r_j = k_0 exp\left(-\frac{E_a}{RT}\right) P_{CO}^{l} P_{H_2O}^{m} P_{CO_2}^{n} P_{H_2}^{q} \left(1 - \frac{1}{K_{eq}} \cdot \frac{P_{CO_2} \cdot P_{H_2}}{P_{CO} \cdot P_{H_2O}}\right)$ (8)

HTSR Reaction Rate: $r_j = k_0 exp\left(-\frac{E_a}{RT}\right) c_{CO}^{l} c_{H_2O}^{m} c_{CO_2}^{n} c_{H_2}^{q} \left(1 - \frac{1}{K_{eq}} \cdot \frac{c_{CO_2} \cdot c_{H_2}}{c_{CO} \cdot c_{H_2O}}\right)$ (9)

$K_{eq} = exp\left(\frac{4577.8}{T} - 4.33\right)$ (10)

model to analyze the MR experimental data. We have utilized an isothermal co-current flow (feed to permeate) model. As can be seen in Fig. 3, the developed multi-scale MR model's predictions capture perfectly the obtained lab-scale experimental data for various weight of catalyst/molar flow rate of CO values. In Fig. 3, the solid-line represents the multi-scale model prediction, while the dots indicate experimental findings.

All reported simulations were carried out with a syngas composition of (H_2/CO/H_2O/CO_2/CH_4/H_2S) = (2.7637/1.00/a/2.1528/0.8/0.05), where 1 < a<5, which is a typical composition of a coal/oxygen-blown gasifier off-gas. We applied the aforementioned empirical power law kinetic rate expressions for the WGSR in all reactor simulations. The corresponding commercial Co/Mo/Al_2O_3 and Fe_2O_3–Cr_2O_3 catalyst's physical properties and characteristics, and the parameters used in the multiscale model's simulations are shown in Tables 3 and 4.

The influence of three catalytic pellet design parameters (volumetric porosity, tortuosity, and mean pore diameter), on the pellet's outer surface molecular fluxes, was investigated for the DGM, MSM, and WM. Given the complexity of a real catalyst pellet's porous structure, which contains networks of pores with very different diameters and layouts, the above parameters represent average values reflecting pore size distribution experimental data. The effect of these parameters on the reaction rate can be seen in Fig. 4 for the HTSR, and LTSR

Table 2 – Properties dependence.

Property description	Dependence in the simulation	
	Pellet	Reactor
Fluid phase viscosity	$\mu_f^p = \mu_f^p(T^p, \{c_i^p\})$	$\mu_f^r = \mu_f^r(T^r, \{c_i^r\})$
Fluid phase conductivity	$\lambda_s^p = \lambda_s^p(T^r)$	$\lambda_f^r = \lambda_f^r(T^r, p^r, \{c_i^r\})$
Binary diffusion coefficients	$D_{ij}^p = D_{ij}^p(T^p, p^p)$	$D_{ij}^r = D_{ij}^r(T^r, p^r)$
Knudsen diffusivities	$D_{iK} = D_{iK}(T^p)$	–
Species i heat capacity	$C_{P,i}^p = C_{P,i}^p(T^p)$	$C_{P,i}^r = C_{P,i}^r(T^r)$
Species i molar enthalpy	$\tilde{h}_{f,i}^p = \tilde{h}_{f,i}^p(T^p)$	$\tilde{h}_{f,i}^r = \tilde{h}_{f,i}^r(T^r)$

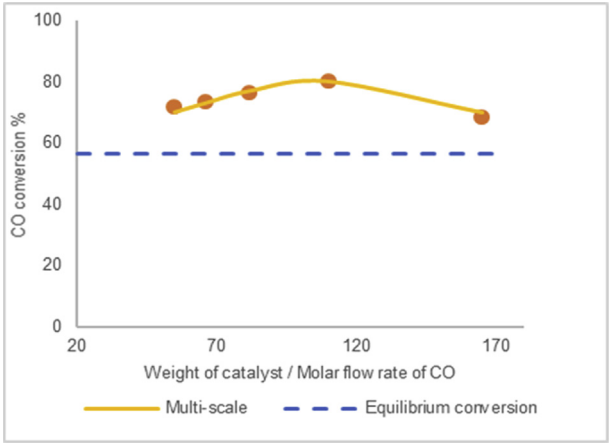

Fig. 3 – Membrane Reactor multi-scale model vs. experimental results at P_{in}:15 bar, T_{in}:523 K.

Table 3 – Parameters used in simulation (LTSR).

Parameter	Value	Dimension
Density of catalyst	592.68	kg/m^3
Pellet void fraction	0.2–0.7	–
Pellet radius	0.004	m
Surface area of catalyst	160-220*10^3	m^2/g
Pore volume of catalyst	0.55–0.65*10^{-6}	m^3/g
Tortuosity	1.4285–5	–
Mean pore diameter	6.3*10^{-7}-10^{-9}	m
Inlet pressure	10–30	bar
Inlet temperature	493–573	K
Reactor length	7	m
Chemical model parameters		
l	0.8	–
m	0.29	–
n	−0.07	–
q	0	–
k_0	6.3	$mol/atm^{l+m+n+q} \cdot h \cdot g$
E_a	5.9	$kcal/mol$

Table 4 – Parameters used in simulation (HTSR).

Parameter	*Value*	*Dimension*
Density of catalyst	1008	kg/m^3
Pellet void fraction	0.2–0.7	–
Pellet radius	0.004	m
Surface area of catalyst	61*10^3	m^2/g
Pore volume of catalyst	0.35*10^{-6}	m^3/g
Tortuosity	1.4285–5	–
Mean pore diameter	6.3*10^{-7}-10^{-9}	m
Inlet pressure	10–40	bar
Inlet temperature	573–673	K
Reactor length	7	m
Chemical model parameters		
l	0.74	–
m	0.47	–
n	−0.18	–
q	0	–
k_0	2623.4	$(m^3/mol)^{l+n+m+q} \cdot s^{-1}$
E_a	80	kJ/mol

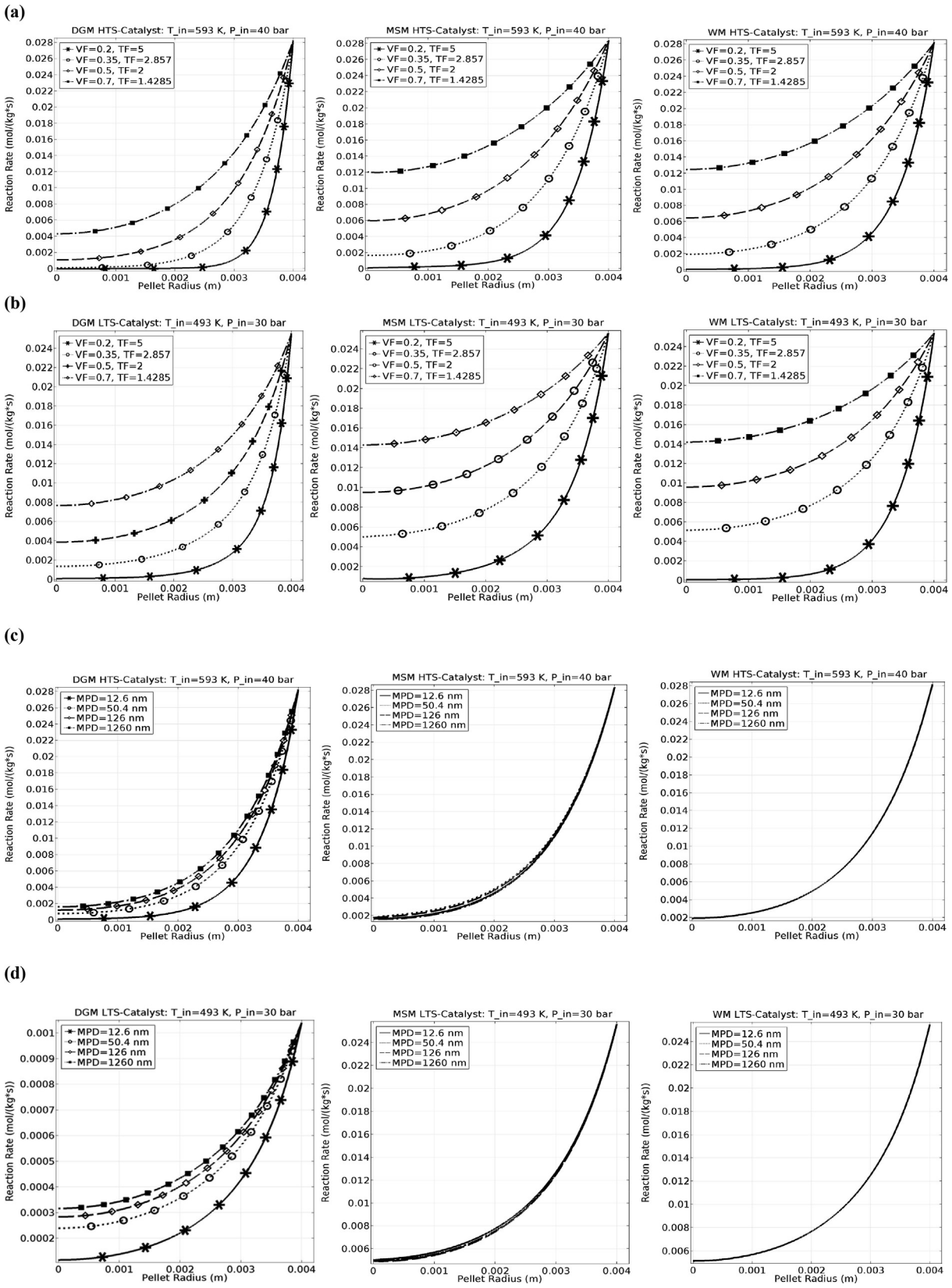

Fig. 4 – Specific generation rate along the pellet radius for various design parameters and flux models. (a) HTS-catalyst mean pore diameter: 12.6 nm. VF=Void Fraction, TF=Tortuosity Factor. (b) LTS-catalyst mean pore diameter: 12.6 nm. VF=Void Fraction, TF=Tortuosity Factor. (c) HTS-catalyst, void fraction=0.35, tortuosity factor=2.857. MPD=Mean Pore Diameter. (d) LTS-catalyst, void fraction=0.35, tortuosity factor=2.857. MPD=Mean Pore Diameter.

catalysts. As expected, the specific generation rate in a fluid phase within the pellet domain increases proportionally to the pellet's volumetric porosity, for both HTSR, and LTSR catalysts. The influence of the pellet's volumetric porosity on the LTSR catalyst is more pronounced than on the HTSR catalyst. The effective Knudsen and bulk diffusivities both decrease, as the tortuosity factor increases, and the pellet void fraction decreases. DGM-based simulations include both the effect of Knudsen and bulk diffusivities, and this influence can clearly be seen in Fig. 4a–b. The Knudsen diffusion flux in the DGM is proportional to the pore size and independent of process pressure. Thus, DGM-based simulation results should demonstrate a dependence of the surface flux on pore diameter. This dependence is indeed shown in Fig. 4c–d, which illustrates the effect of the mean pore diameter on the effective reaction rate along the pellet's radius. On the other hand, the effective bulk diffusivities are independent of pore size and inversely propositional to pressure, so both the MSM and WM don't capture Knudsen diffusion. As illustrated in Fig. 4c–d, the MSM and WM-based simulations indeed do not exhibit any dependence on the mean pore diameter and provide similar effective reaction rate predictions. Since the DGM predictions exhibit significant deviations to the MSM-WM ones (Fig. 4a–b), it is thus prudent to suggest that use of the DGM is preferable to the use of MSM-WM, for both HT and LT catalysts' modeling, especially when Knudsen diffusion is not negligible.

The influence of the different flux diffusion models on the H_2 mole fraction along the reactor length and pellet radius, for both the HTSR and LTSR, is depicted in Fig. 5a–b.

The influence of the different flux diffusion models on the H_2 mole fraction along the reactor length and pellet radius, for both the HTSR and LTSR, is depicted in Figs. 8 and 9. The aforementioned H_2 axial and radial profiles are overestimated by the WM compared to the DGM and MSM. Further, the overall reactor scale results suggest that Knudsen diffusion is more dominant in the HTS catalyst compared to the LTS catalyst. However, the rigorous DGM and MSM are approximately 30% and 80% more computationally expensive than the WM. The equimolar nature of products and reactants in the WGSR, and the steady-state operation requirement, suggest that the total molar flux sum, and the mass averaged velocity must both be equal to zero for every pellet radial position. These requirements serve as simulation consistency checks and are found to be satisfied to within the employed numerical accuracy. Based on the averaged mass and molar velocities, it is easy to see that the diffusion fluxes clearly dominate over the convective fluxes. As a result, neglecting the convective flux terms in the diffusion.

The aforementioned H_2 axial and radial profiles are overestimated by the WM compared to the DGM and MSM. Further, the overall reactor scale results suggest that Knudsen diffusion is more dominant in the HTS catalyst compared to the LTS catalyst. However, the rigorous DGM and MSM are

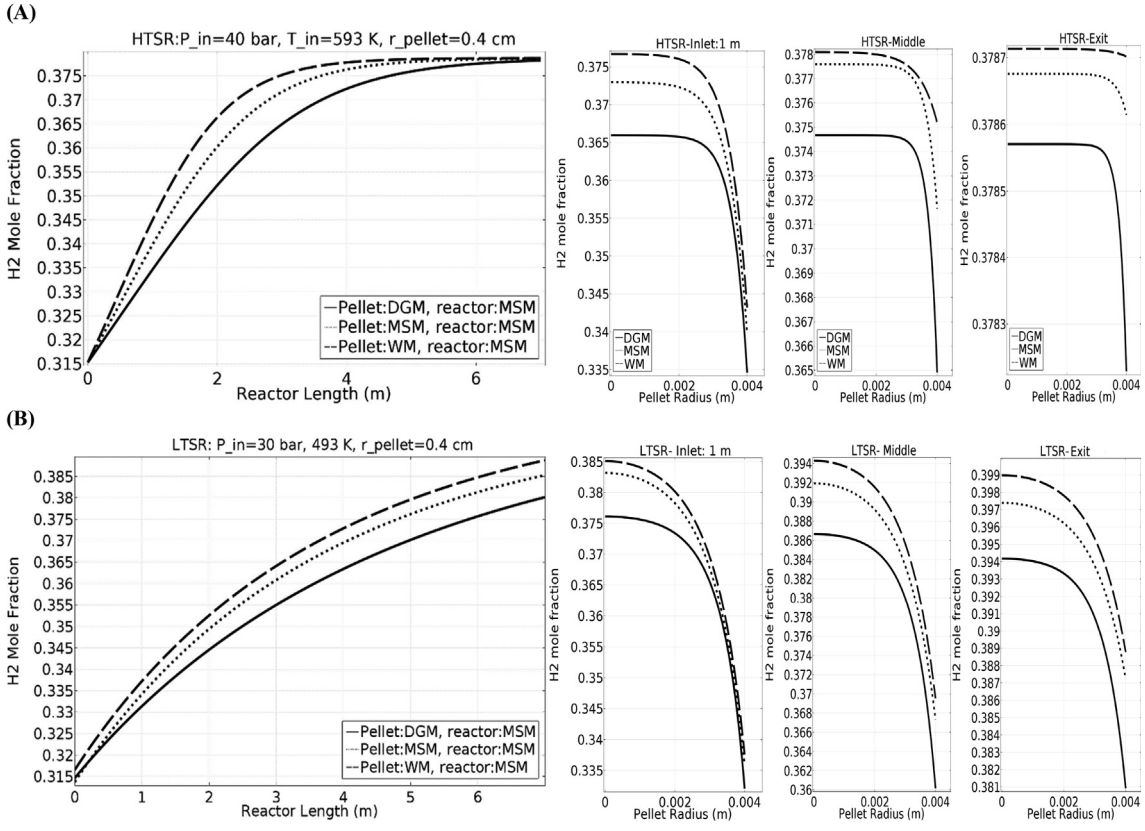

Fig. 5 – H_2 mole fraction along the reactor length (Left) and pellet radius (Right) for various reactor positions, mean pore diameter: 12.6 nm, void fraction:0.35, and (A) P_in = 40 bar, T_in = 593K (B) P_in = 30 bar, T_in = 493K.

approximately 30% and 80% more computationally expensive than the WM. The equimolar nature of products and reactants in the WGSR, and the steady-state operation requirement, suggest that the total molar flux sum, and the mass averaged velocity must both be equal to zero for every pellet radial position. These requirements serve as simulation consistency checks and are found to be satisfied to within the employed numerical accuracy. Based on the averaged mass and molar velocities, it is easy to see that the diffusion fluxes clearly dominate over the convective fluxes. As a result, neglecting the convective flux terms in the diffusion models is a reasonable assumption. The following conclusions are established for the reactor operating conditions used in the present work. Within the catalyst pellet domain, isothermal and isobaric conditions can be assumed, and convective fluxes are much lower than diffusive fluxes, and can thus be neglected. Outside the catalyst pellet domain, temperature gradients are not negligible, and must therefore be solved for by the model simulations.

Unlike most WGSR literature studies, which assume constant catalyst pellet effectiveness factors, this work employs the DGM to quantify the effectiveness factor for pellets situated along the HTSR and LTSR axes. Given the WGSR stoichiometry, all species' effectiveness factors are equal. Fig. 6 demonstrates that at any fixed axial HTSR/LTSR adiabatic reactor location, the effectiveness factor decreases as the pellet void fraction is reduced. Further, the effectiveness factor decreases along both the HTSR and LTSR lengths, because the reacting mixture's temperature increases axially, thus accelerating the intrinsic WGSR kinetics more than the species' diffusivities, which in turn increases the effectiveness factor's denominator more than its numerator. On the other hand, the mean pore diameter, at the considered values, doesn't have a significant effect on the effectiveness factor for both the HTSR and the LTSR.

Alternative intensified reactor-separator design results

In the remainder of this work, the DGM is used as the molecular flux model at the pellet scale, while the MSM is used at the reactor scale. As shown in Fig. 1, three alternative designs are considered for carrying out the WGSR, within IGCC and gas fired power plants. The conventional process is carried out in a HTSR-Cooler-LTSR sequence. A number of simulations are carried-out for this system, which is used as the baseline to which our proposed MR/MS-based designs will be compared. CO conversion is employed as the comparative performance criterion for all considered designs. Fig. 7a illustrates CO conversion along the combined HTSR/LTSR reactor's length of the baseline design, for various operating conditions. The obtained simulation results suggest (consistent with industry) that CO conversion reaches 95%, if the adiabatic HTSR's inlet conditions are kept at 593 K, and H_2O/CO ratio of 5, and the adiabatic LTSR's inlet temperature is kept at 493 K. Thus, the total CO conversion of 95% is chosen as the key design specification that must be met by the baseline and alternative processes.

Fig. 7b shows the temperature profiles along the combined reactor's length (HTSR/LTSR). In our multi-scale model, we calculated the temperature profiles of the catalyst-pellet and bulk gas phases in both the HTSR and LTSR. Minimum and maximum temperature differences, between the bulk gas phase and catalyst pellet, along the reactor length for the adiabatic reactor simulations can be expressed as 2–0.02 K (WM), 1.55–0.035 K (MSM), 1.2–0.05 K (DGM) for HTSR, and 2.8–0.3 K (WM), 2.7–0.25 K (MSM), 2.1–0.5 K (DGM) for LTSR.

The simultaneous reaction/separation nature of the considered alternative designs, qualifies them as intensifying processes for the baseline design. Process intensification (PI) encompasses any chemical engineering development offering drastic improvements, in regard to a variety of metrics. Such

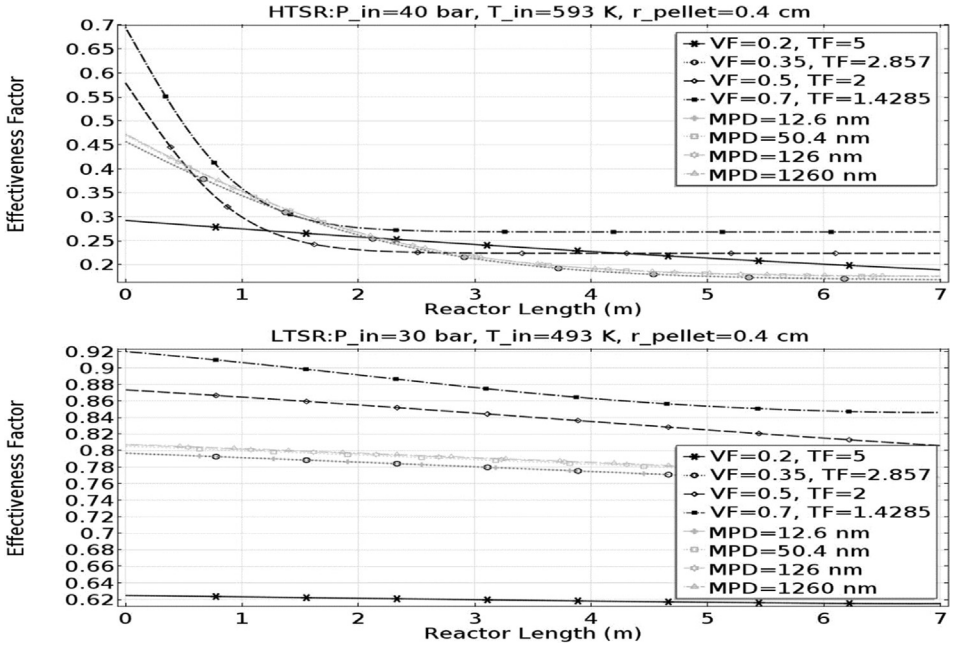

Fig. 6 – Effectiveness factor axial profiles for various design parameters, VF: void fraction and MPD: mean pore diameter. (HTSR-Up and LTSR-Down).

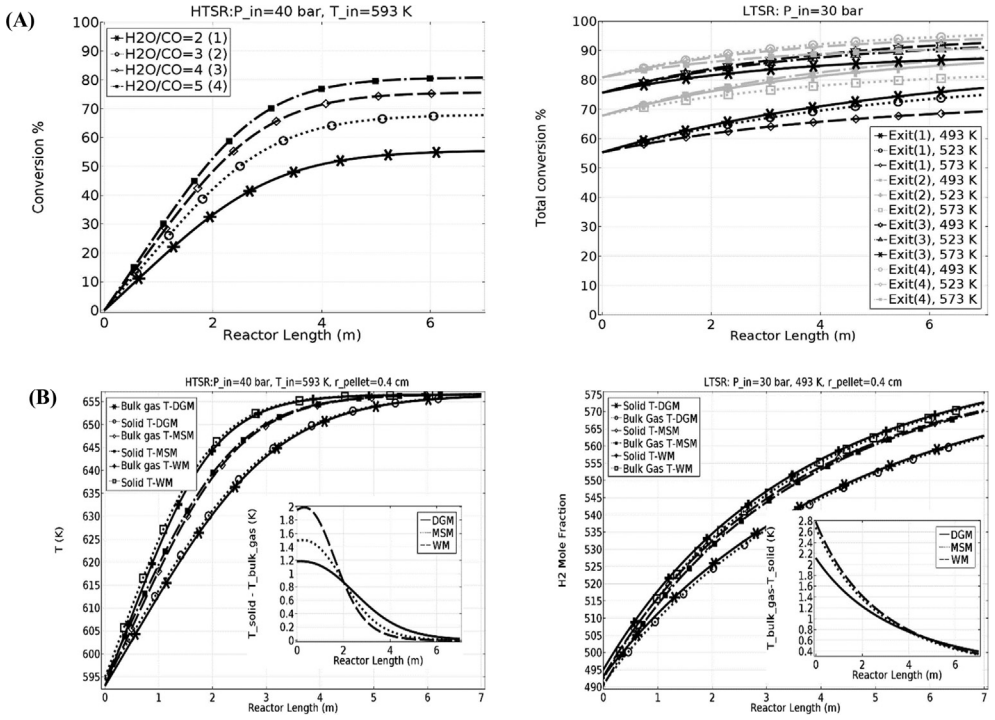

Fig. 7 – Combined HTSR and LTSR system's (A) conversion evaluation along the combined reactor's length*. (B) temperature profiles evaluations along the combined reactor's length for industrial scale application.* The resulting HTSR's exit for the cases (1), (2), (3) and (4) is fed into the LTSR for each set of simulation conditions 493 K, 523 K and 573 K.

intensification has the potential to improve process efficiency and economics. As part of the intensification procedure, integration of multiple operations (e.g., reaction and separation) is used as a robust tool to improve the existing process' efficiency, and to reduce energy consumption, and unwanted output/by-product formation [5–7]. In this study, we chose the reduction of reactive volume (catalyst amount) and the increase of H_2 production rate, as process intensification metrics and comparison criteria among the three design alternatives. In this comparative evaluation, total CO conversion is fixed at 95% for all designs.

In the first alternative process, a membrane separator (MS) is placed at the HTSR exit, to separate H_2 from the HTSR exit stream and to subsequently feed its retentate stream to the LTSR. This H_2 separation creates a synergy that significantly increases overall process efficiency and results in higher conversion. Since membrane area has a significant impact on the MS/MR's performance, and is also a key contributing component to the MS/MR capital cost, several simulations have been carried out, for various MS H_2 production levels (i.e. 60%, 75%, and 90% of the H_2 produced in the HTSR, being separated in the MS as pure product). The same procedure is applied to LTMRs (with 60%, 75% and 90% of the H_2 produced in the first LTMR, being separated as pure product. A process performance of having >90% H_2 separation in total is attained by all three designs. The summary of process conditions, process outcomes, and intensification metrics for the conventional process, alternative process 1, and alternative process 2, is depicted in Fig. 8.

Fig. 9 represents CO conversion along the HTSR-MS-LTSR system. As can be seen in Fig. 9 (Right), intermediate MS H_2 separation levels increase total CO conversion by approximately 9% (60% H_2 separation), 12% (75% H_2 separation) and 17% (90% H_2 separation). Moreover, the HTSR-MS-LTSR system reaches the 95% total CO conversion criterion for HTSR H_2O/CO ratios of 3 and 4, which are lower than the H_2O/CO ratio of 5 that must be utilized by the conventional system to reach the same total CO conversion.

The use of MR technology for the WGSR, offers unique advantages that include WGSR equilibrium conversion and kinetic rate enhancement through hydrogen removal, high-purity hydrogen production, lower operating temperatures and steam requirements, reduced catalyst use, increased operation safety, and elimination of downstream hydrogen purification. The employed MR multi-scale model captures these advantageous process characteristics through repeated application of the Reynolds Transport Theorem (RTT) to each of the MR domains: the pellet domain, the reactor domain, and the permeation zone domain [21].

An industrial scale membrane reactor consists of a pressure vessel that houses several membrane bundles, each bundle consisting of multiple CMS membrane tubes. These bundles typically consist of CMS membrane tubes, whose dimensions are an inner and outer diameter of 3.5 mm and 5.7 mm respectively, and a length of 1 m (Fig. 10). A typical large-scale MR consists of several (e.g. 1400) bundles in parallel (1 m each in length) and a scalar multiple of that number of bundles in total (e.g. 9800 for a 7 m long MR), as illustrated in

	Process Conditions	Process Outcomes	Intensification Metrics
Conventional Process (Baseline)	*1- HTSR-adiabatic (593 K, 40 bar and $H_2O/CO=5$)* *2- Cooling to 493 K* *3- LTSR-adiabatic (493 K, 30 bar)*	*95% Conversion* *(baseline-used catalyst amount and produced H_2 rate are calculated)*	*Catalyst Amount Metric=1 (baseline)* *H_2 Production Rate Metric=1 (baseline)*
Proposed Process 1 (HTSR/MS/LTSR/MS)	*1- HTSR-adiabatic (593 K, 40 bar)* *2- Membrane separation of 60%, 75% and 90%-H_2 (obtained at the exit HTSR)* *3- Cooling to 493 K* *4- LTSR-adiabatic (493 K, 30 bar)* 5- Membrane *separation of H_2 to reach total >90% separation*	*95% Conversion* *>90% H_2 Separation* *(1- Fix H_2 production rate as baseline and calculate the reduction in the amount of catalyst* *2- Fix the amount of catalyst as baseline and calculate the increase in H_2 production rate)*	*Catalyst Amount Metric=0.89 (60% H_2 separation), 0.8 (75% H_2 separation) and 0.68 (90% H_2 separation)* *H_2 Production Rate Metric=1.15 (60% H_2 separation), 1.45 (75% H_2 separation) and 1.7 (90% H_2 separation)*
Proposed Process 2 (LTMR/LTMR)	*1- LTMR-adiabatic (523 K, 40 bar) and separation of 60%, 75% and 90%-H_2* *2- Cooling to 523 K* *3- LTMR-adiabatic (523 K) and separation of H_2 to reach total >90% separation*	*95% Conversion* *>90% H_2 Separation* *(1- Fix H_2 production rate as baseline and calculate the reduction in the amount of catalyst* *2- Fix the amount of catalyst as baseline and calculate the increase in H_2 production rate)*	*Catalyst Amount Metric=0.61 (60% H_2 separation), 0.56 (75% H_2 separation) and 0.45 (90% H_2 separation)* *H_2 Production Rate Metric=1.22 (60% H_2 separation), 1.55 (75% H_2 separation) and 1.9 (90% H_2 separation)*

Fig. 8 – Summary of process conditions, process outcomes and intensification metrics.

Figure 13.60%, 75% and 90% of the H_2 produced in the first LTMR is separated, by varying the number of tubes in the first LTMR and then feeding the LTMR's reject side to the second LTMR. Again, above 90% H_2 separation is achieved in the third alternative process.

The MR simulations are carried out with feed syngas composition identical to that used for the conventional process. In the simulations, the membrane permeances (m^3/m^2.h.bar) were taken to be: $H_2 = 1$; $CO = 0.0125$; $CO_2 = 0.025$; $CH_4 = 0.00806$, $H_2O = 0.333$, which are typical of values measured in high-quality CMS membranes prepared by Media and Process Technology, Inc [2]. The derivation of the MR model equations can be found in [21]. In the MS simulations, the same membrane characteristics are employed, and simply the reaction (catalyst) effect is removed from the process model.

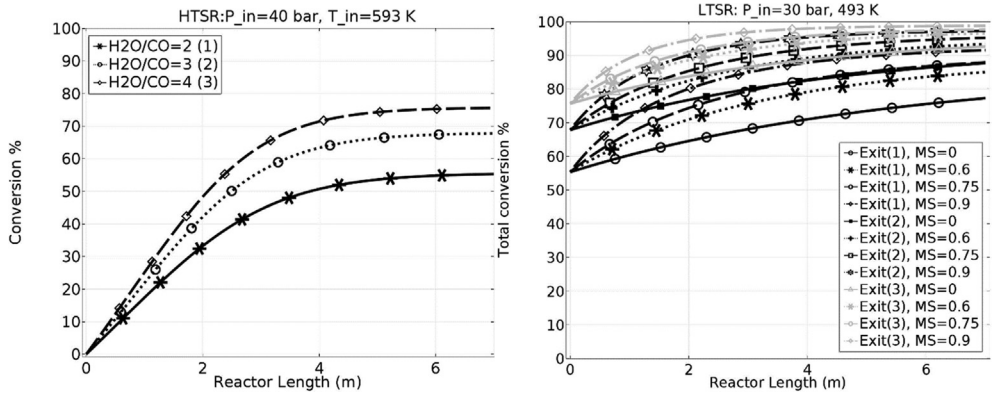

Fig. 9 – Multistage (HTSR/MS/LTSR/MS) system's conversion evaluation along the combined reactor's length*. * The resulting HTSR's exit for the cases (1), (2) and (3) is fed into the LTSR for each set of simulation conditions of 0%, 60%, 75%, and 90% H_2 (produced in the HTSR and separated in the intermediate MS) separation.

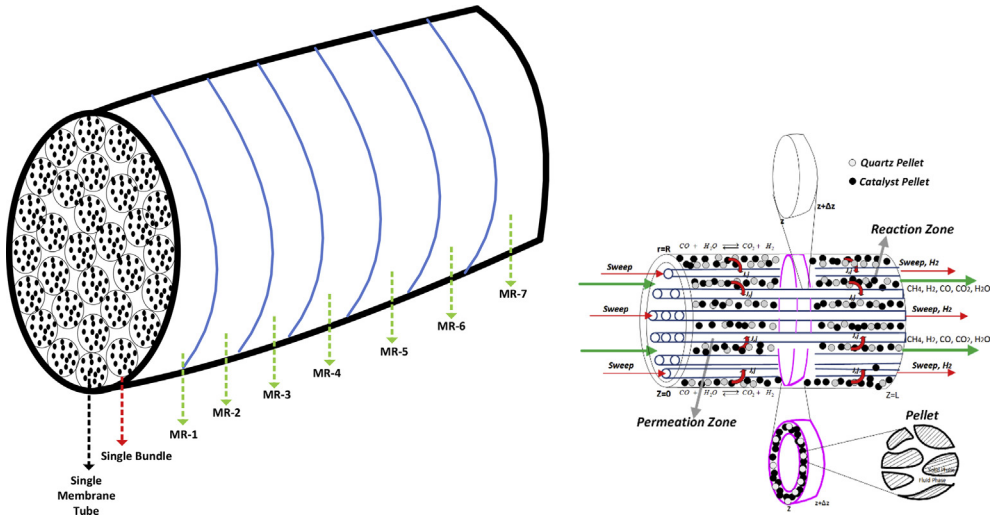

Fig. 10 – A schematic of the configuration for the sequence of MRs and 1-D Representation of control volumes in a Membrane Reactor.

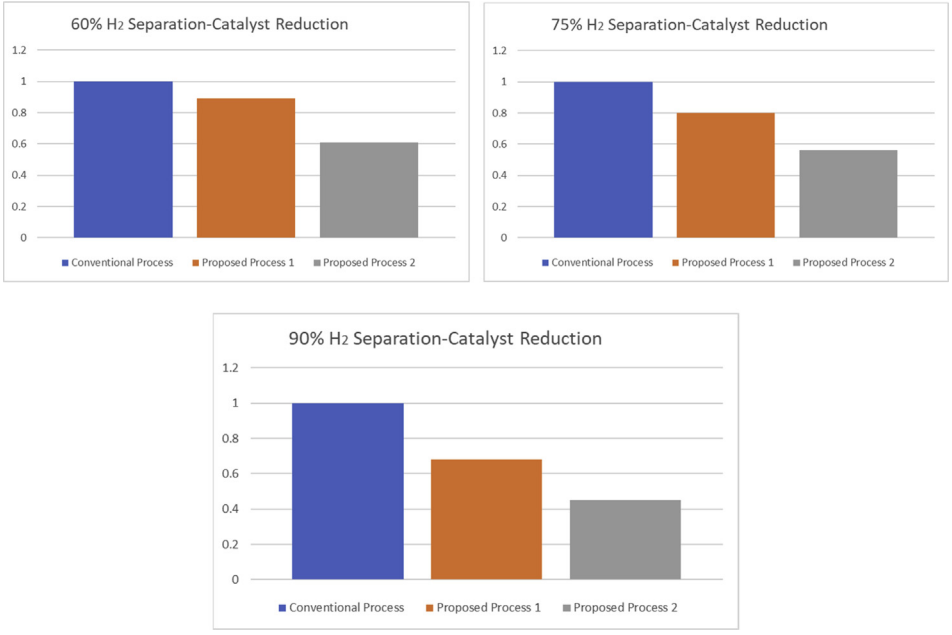

Fig. 11 – Process catalyst amount reduction for various H_2 separation factors.

The catalyst amount reduction for all designs is depicted in Fig. 11 for various intermediate H_2 separation levels of 60%, 75% and 90%. The H_2 production rate is kept constant to obtain these results. Approximately 11% (conventional→ proposed 1)/18% (conventional→ proposed 2), 20% (conventional→ proposed 1)/25% (conventional→ proposed 2), and 32% (conventional→ proposed 1)/40% (conventional→ proposed 2) of reactive volume reduction is obtained for the H_2 separation levels of 60%, 75% and 90%, respectively. Similarly, approximately 11% (conventional→ proposed 1)/39% (conventional→ proposed 2), 20% (conventional→ proposed 1)/44% (conventional→ proposed 2) and 32% (conventional→ proposed 1)/55% (conventional→ proposed 2) of catalyst amount reduction is obtained for the H_2 separation levels of 60%, 75% and 90%, respectively.

The H_2 production rate increase (for constant amount of catalyst) for the three hydrogen production systems is shown in Fig. 12 for various H_2 separation levels of 60%, 75% and 90%. Transitioning from the conventional process to the proposed 1 and proposed 2 processes increases the H_2 production rate 15%–22% for 60% separation, 45%–55% for 75% separation, and 70%–90% for 90% separation.

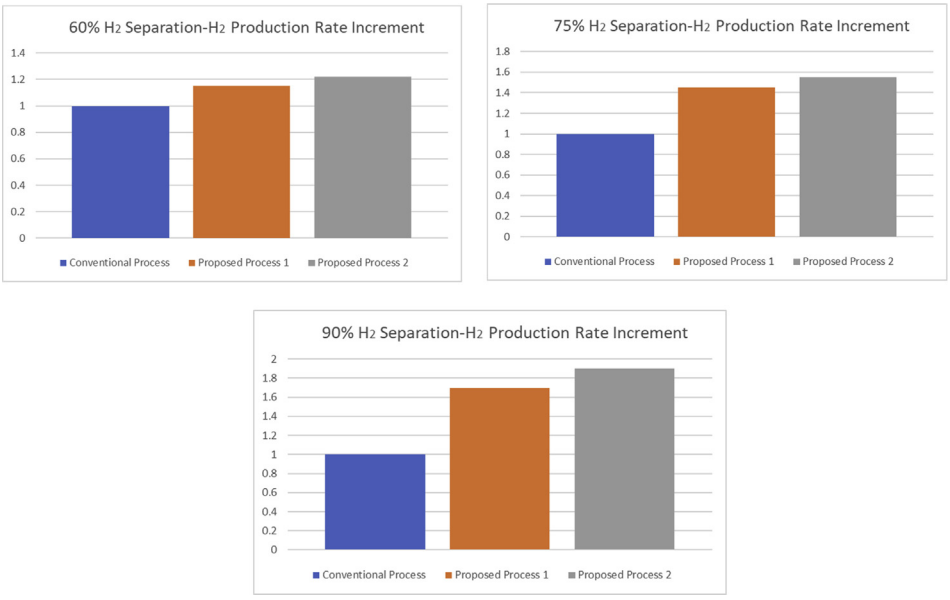

Fig. 12 – Process H_2 production rate increment for various H_2 separation factors.

Conclusions

Various local design parameters and species' flux models (MSM, WM, DGM) are employed in deriving a multi-scale reactive-separator mathematical model that can predict the performance of WGSR-based hydrogen production systems. The following results are obtained:

(1) For various pellet-scale design parameters (mean pore diameter, volumetric porosity, tortuosity factor), the prediction of the MSM and WM are close to each other for both HT and LT catalysts. However, significant deviations are observed from MSM-WM to DGM, for catalytic pellets with small pore diameters for which Knudsen diffusion is significant. The DGM is subsequently employed for all subsequent pellet scale simulations, to ensure accuracy.
(2) The calculated H_2 mole fraction axial profiles, for the considered flux models, suggest that the WM overestimates H_2 mole fractions compared to both the DGM (average excess estimations are 2.78% for LTSR and 2.6% for HTSR) and the MSM (average excess estimations are 1.31% for LTSR and 1.1% for HTSR). However, the rigorous DGM and MSM are approximately 30% and 80% more computationally expensive than the WM.
(3) The DGM and the aforementioned pellet-scale design parameters enable the calculation of catalyst pellet effectiveness factors throughout the reactor, and indicate significant effectiveness factor spatial variations.
(4) Two process intensifying alternative WGSR designs are proposed. The multi-scale simulation results show that both proposed alternative processes 1 and 2 are superior to the conventional process, in regard to several intensification metrics.

Acknowledgements

Financial support through DOE grant DE-FE0026423 "A High Efficiency Ultra-Compact Process for Pre-Combustion CO2 Capture" is gratefully acknowledged. Financial support from The Republic of Turkey Federal Agency for Support and Evaluation of Graduate Education within the Ministry of Education of Turkey is also gratefully acknowledged.

Notation

English Symbols

$A^p(m^2\ of\ domain\ p)$ Area of the control surface of domain p

$A_c^r(m^2)$ Cross section area of the tubular reactor

$B_O(m^2)$ Viscous flow parameter of domain p

$c_{\gamma,i}^{\alpha}\left(\frac{mol\ of\ species\ i\ \ in\ \ phase\ \gamma\ within\ domain\ \alpha}{m^3\ of\ phase\ \gamma\ within\ domain\ \alpha}\right)$ Species'i molar density of phase γ within domain α

$c_{\gamma,tot}^{\alpha}\left(\frac{mol\ of\ phase\ \gamma\ within\ domain\ \alpha}{m^3\ of\ phase\ \gamma\ within\ domain\ \alpha}\right)$ Total molar density of phase γ within domain α

$C_{P,i}^{\alpha}\left(\frac{J\ \ of\ species\ i\ \ in\ \ phase\ \gamma\ within\ domain\ \alpha}{(mol\cdot K)of\ the\ \ i^{th}\ component\ of\ \ phase\ \gamma\ within\ domain\ \alpha}\right)$ Species' i molar specific heat at constant pressure of phase f within domain α

$C_V^{\alpha}\left(\frac{J\ \ phase\ s\ within\ domain\ \alpha}{(mol\cdot K)of\ \ phase\ s\ within\ domain\ \alpha}\right)$ Species' i molar specific heat at constant volume of phase s within domain α

$CS^{\alpha}(m^2\ of\ domain\ \alpha)$ Control surface of domain α

$CV^{\alpha}(m^3\ of\ domain\ \alpha)$ Control volume of domain α

$D_{ij}^{\alpha}\left(\frac{m^2\ of\ phase\ f\ within\ of\ domain\ \alpha}{s}\right)$ Species' i and j binary diffusion coefficient of phase γ within domain α

$D_{ij}^{eff}\left(\frac{m^2\ of\ domain\ p}{s}\right)$ Species' i and j effective binary diffusion coefficient in domain p

$D_{iK}\left(\frac{total\ m^2\ of\ domain\ p}{s}\right)$ Species' i Knudsen diffusion coefficient in domain p

$\tilde{D}_{i}^{r}\left(\frac{m^2\ of\ phase\ f\ within\ domain\ r}{s}\right)$ Species' i thermal diffusion coefficient of phase f within domain r

$d^{p}(m)$ Diameter of the catalytic pellet

$d_{pore}^{p}(m)$ Mean pore diameter in domain p

$d^{r}(m)$ Diameter of the tubular reactor

$h^{\alpha}\left(\frac{J\ from\ phase\ f\ within\ domain\ \alpha}{((m^2 \cdot K)\ of\ phase\ s\ within\ domain\ \alpha)\cdot s}\right)$ Interfacial heat transfer coefficient between phase f within domain α and phase s within domain α

$H_{\gamma}^{\alpha}\left(\frac{J\ of\ phase\ \gamma\ within\ domain\ \alpha}{kg\ of\ phase\ \gamma\ within\ domain\ \alpha}\right)$ Mass specific enthalpy of phase γ within domain α

$\tilde{H}_{i}^{0}\left(\frac{J\ of\ species\ i\ \ in\ phase\ f}{mol\ of\ species\ i\ \ in\ phase\ f}\right)$ Species' i standard molar enthalpy of formation

$\tilde{h}_{\gamma,i}^{\alpha}\left(\frac{J\ of\ phase\ \gamma\ within\ domain\ \alpha}{mol\ of\ phase\ \gamma\ within\ domain\ \alpha}\right)$ Species' i molar enthalpy of phase γ within domain α

$k_{\gamma}^{\alpha}\left(\frac{J\ of\ phase\ \gamma\ within\ domain\ \alpha}{((m \cdot K)\ of\ phase\ \gamma\ within\ domain\ \alpha)\cdot s}\right)$ Thermal conductivity of phase γ within domain α

$\overrightarrow{j_{\gamma,i}^{\alpha}}\left(\frac{mol\ of\ species\ i\ \ in\ \ phase\ \gamma\ within\ domain\ \alpha}{(m^2\ of\ phase\ \gamma\ within\ domain\ \alpha)\cdot s}\right)$ i^{th} species diffusion molar flux in phase γ within domain α

$\overrightarrow{J_{\gamma,i}^{\alpha}}\left(\frac{mol\ of\ species\ i\ \ in\ \ phase\ \gamma\ within\ domain\ \alpha}{(m^2\ of\ phase\ \gamma\ within\ domain\ \alpha)\cdot s}\right)$ i^{th} species combined diffusion-convection mass flux in phase γ within domain α

$L^{r}(m)$ Length of the tubular reactor

$M_{i}\left(\frac{kg\ of\ i}{mol\ of\ i}\right)$ i^{th} species molar mass

$\overrightarrow{n}$ (*dimensionless*) Unit vector direction of the differential areadA of the CS

$\overrightarrow{n_{\gamma,i}^{\alpha}}\left(\frac{kg\ of\ species\ i\ \ in\ \ phase\ \gamma\ within\ domain\ \alpha}{(m^2\ of\ phase\ \gamma\ within\ domain\ \alpha)\cdot s}\right)$ i^{th} species diffusion mass flux in phase γ within domain α

$\overrightarrow{N_{\gamma,i}^{\alpha}}\left(\frac{kg\ of\ species\ i\ \ in\ \ phase\ \gamma\ within\ domain\ \alpha}{(m^2\ of\ phase\ \gamma\ within\ domain\ \alpha)\cdot s}\right)$ i^{th} species combined diffusion-convection mass flux in phase γ within domain α

$p^{\alpha}\left(\frac{J\ of\ phase\ f\ within\ domain\ \alpha}{m^3\ of\ phase\ f\ within\ domain\ \alpha}\right)$ Pressure of phase γ within domain α

$\overrightarrow{Q_{\gamma}^{\alpha}}\left(\frac{J\ of\ phase\ \gamma\ within\ domain\ \alpha}{(m^2\ of\ phase\ \gamma\ within\ domain\ \alpha)\ \cdot s}\right)$ Heat flux into phase γ within domain α

$\overrightarrow{q_{f\rightarrow s}^{\alpha}}\left(\frac{J\ from\ phase\ f\ to\ s\ within\ domain\ \alpha}{(m^3\ of\ domain\ \alpha)\ \cdot s}\right)$ Heat transferred from phase f to s within domain α

$\overrightarrow{q_{c}^{r}}\left(\frac{J\ from\ \ domain\ \ r\ \ to\ domain\ p}{(m^3\ of\ domain\ \ r)\ \cdot s}\right)$ Heat transferred from domain r to domain p due to convection

$\overrightarrow{q_{m}^{r}}\left(\frac{J\ from\ \ domain\ \ r\ \ to\ domain\ p}{(m^3\ of\ domain\ \ r)\ \cdot s}\right)$ Heat transferred from domain r to domain p due to mass flux

$R_{\gamma,i}^{\alpha}\left(\frac{mols\ of\ species\ i\ in\ phase\ \gamma\ within\ domain\ \alpha}{(m^3\ of\ domain\ \alpha)\ \cdot s}\right)$ i^{th} species volumetric generation rate in phase γ within domain α

$\overline{R}_{f,i}^{p}\left(\frac{mols\ of\ species\ i\ in\ phase\ f\ within\ domain\ p}{(kg\ of\ phase\ s\ within\ domain\ p)\ \cdot s}\right)$ i^{th} species phase s specific generation rate in phase f within domain p

$\tilde{R}\left(\frac{J}{mol.K}\right)$ Universal gas constant

$r(m\ of\ domain\ p)$ spatial variable of domain p

$r^{p}(m)$ Radius of the pellet

$\overrightarrow{S_{\gamma}^{\alpha}}\left(\frac{kg\ of\ phase\ \gamma\ within\ domain\ \alpha}{(m^2\ of\ domain\ \alpha)\cdot s^2}\right)$ Momentum source term of phase γ within domain α

$\tilde{S}_{\gamma\rightarrow\gamma'}^{\alpha}\left(\frac{J\ of\ phase\ \gamma\ to\ \gamma'\ within\ domain\ \alpha}{(m^3\ of\ domain\ \alpha)\cdot s^2}\right)$ Interphase energy transfer source term in domain α

$T_{\gamma}^{\alpha}(K)$ Temperature of phase γ within domain α

$T^{p}(K)$ Temperature of the composite phase in domain p

$T^{w}(K)$ Temperature of inner wall of the tubular reactor

$\overrightarrow{\overrightarrow{T_{\gamma}^{\alpha}}}\left(\frac{kg\ of\ phase\ \gamma\ within\ domain\ \alpha}{(m\ of\ phase\ \gamma\ within\ domain\ \alpha)\cdot s^2}\right)$ Viscous momentum flux tensor of phase γ within domain α

$V^{p}(m^3\ of\ domain\ p)$ Total volume of domain p

$\overrightarrow{v_{\gamma}^{\alpha}}\left(\frac{m}{s}\right)$ Mass average velocity of the phase γ within domain α

$\overrightarrow{v_{\gamma,i}^{\alpha}}\left(\frac{m}{s}\right)$ i^{th} species velocity in phase γ within domain α

$w_{\gamma,i}^{\alpha}\left(\frac{kg\ of\ species\ i\ \ in\ \ phase\ \gamma\ within\ domain\ \alpha}{kg\ of\ \ phase\ \gamma\ within\ domain\ \alpha}\right)$ i^{th} species mass fraction in phase γ within domain α

$x_{\gamma,i}^{\alpha}\left(\frac{mol\ of\ species\ i\ in\ phase\ \gamma\ within\ domain\ \alpha}{mol\ of\ phase\ \gamma\ within\ domain\ \alpha}\right)$ i^{th} species molar fraction in phase γ within domain α

Greek symbols

$\varepsilon_{\gamma,V}^{\alpha}\left(\frac{m^3\ of\ phase\ \gamma\ within\ domain\ \alpha}{total\ m^3\ of\ domain\ \alpha}\right)$ Volumetric fraction of phase γ within domain α

$\varepsilon_{\gamma,A}^{\alpha}\left(\frac{m^2\ of\ phase\ \gamma\ within\ domain\ \alpha}{total\ m^2\ of\ domain\ \alpha}\right)$ Surface fraction of phase γ within domain α

$\rho_{\gamma}^{\alpha}\left(\frac{kg\ of\ phase\ \gamma\ within\ domain\ \alpha}{m^3\ of\ phase\ \gamma\ within\ domain\ \alpha}\right)$ Mass density of phase γ within domain α

$\rho_{\gamma,i}^{\alpha}\left(\frac{kg\ of\ species\ i\ in\ phase\ \gamma\ within\ domain\ \alpha}{m^3\ of\ phase\ \gamma\ within\ domain\ \alpha}\right)$ i^{th} species mass concentration in phase γ within domain α

$\tau\left(\frac{m\ \ of\ diffusion\ path\ length\ in\ phase\ f\ within\ domain\ p}{m\ \ of\ CV\ length\ in\ domain\ p}\right)$ Tortuosity of phase$f$ within domain p

$\mu_{f}^{\alpha}\left(\frac{kg\ of\ \ species\ i\ in\ phase\ \gamma\ within\ domain\ \alpha}{(m\ of\ phase\ \gamma\ within\ domain\ \alpha)\cdot s}\right)$ Viscosity of phase f within domain $\alpha 0$

υ(*dimensionless*) Total number of species in the phase-domain

REFERENCES

[1] Harale A, Hwang HT, Liu PK, Sahimi M, Tsotsis TT. Design aspects of the cyclic hybrid adsorbent-membrane reactor (HAMR) system for hydrogen production. Chem Eng Sci 2010;65(1):427–35.

[2] Garshasbi A, Chen H, Cao M, Karagöz S, Ciora Jr RJ, Liu PK, Manousiouthakis VI, Tsotsis TT. Membrane-based reactive separations for process intensification during power generation. Catal Today 2017;331:18–29.

[3] Amadeo NE, Laborde MA. Hydrogen production from the low-temperature water-gas shift reaction: kinetics and simulation of the industrial reactor. Int J Hydrogen Energy 1995;20(12):949–56.

[4] Adrover ME, López E, Borio DO, Pedernera MN. Simulation of a membrane reactor for the WGS reaction: pressure and thermal effects. Chem Eng J 2009;154(1):196–202.

[5] Ding OL, Chan SH. Water–gas shift reaction–A 2-D modeling approach. Int J Hydrogen Energy 2008;33(16):4325–36.

[6] Martos C, Dufour J, Ruiz A. Synthesis of Fe_3O_4-based catalysts for the high-temperature water gas shift reaction. Int J Hydrogen Energy 2009;34(10):4475–81.

[7] Lukyanov BN, Andreev DV, Parmon VN. Catalytic reactors with hydrogen membrane separation. Chem Eng J 2009;154(1):258–66.

[8] Kim GY, Mayor JR, Ni J. Parametric study of microreactor design for water gas shift reactor using an integrated reaction and heat exchange model. Chem Eng J 2005;110(1):1–10.

[9] Choi Y, Stenger HG. Water gas shift reaction kinetics and reactor modeling for fuel cell grade hydrogen. J Power Sources 2003;124(2):432–9.

[10] Giunta P, Amadeo N, Laborde M. Simulation of a low-temperature water gas shift reactor using the heterogeneous model/application to a pem fuel cell. J Power Sources 2006;156(2):489–96.

[11] Ayastuy JL, Gutierrez-Ortiz MA, González-Marcos JA, Aranzabal A, Gonzalez-Velasco JR. Kinetics of the low-temperature WGS reaction over a CuO/ZnO/Al2O3 catalyst. Ind Eng Chem Res 2005;44(1):41–50.

[12] Chen WH, Lin MR, Jiang TL, Chen MH. Modeling and simulation of hydrogen generation from high-temperature and low-temperature water gas shift reactions. Int J Hydrogen Energy 2008;33(22):6644–56.

[13] Lund CR. Water-gas shift kinetics over iron oxide catalysts at membrane reactor conditions. Final Rep Chem Eng Dep Univ Buffalo 2002. 14260-14200.

[14] Smith RJ, Loganathan M, Shantha MS. A review of the water gas shift reaction kinetics. Int J Chem React Eng 2010;8(1).

[15] Newsome DS. The water-gas shift reaction. Catal Rev Sci Eng 1980;21(2):275–318.

[16] Ayturk ME, Kazantzis NK, Ma YH. Modeling and performance assessment of Pd-and Pd/Au-based catalytic membrane reactors for hydrogen production. Energy Environ Sci 2009;2(4):430–8.

[17] Basile A, Paturzo L, Galucci F. Co-current and counter-current modes for water gas shift membrane reactor. Catal Today 2003;82:275–81.

[18] Piemonte V, De Falco M, Basile A. Performance assessment of water gas shift membrane reactors by a two-dimensional model. Energy Sources, Part A Recovery, Util Environ Eff 2015;37(20):2174–82. https://doi.org/10.1080/15567036.2012.691945.

[19] Basile A, Curcio S, Bagnato G, Liguori S, Jokar SM, Iulianelli A. Water gas shift reaction in membrane reactors: theoretical investigation by artificial neural networks model and experimental validation. Int J Hydrogen Energy 2015;40:5897–906.

[20] da Cruz FE, Karagöz S, Manousiouthakis VI. Parametric studies of steam methane reforming using a multiscale reactor model. Ind Eng Chem Res 2018;56(47):14123–39.

[21] Karagöz S, da Cruz FE, Tsotsis TT, Manousiouthakis VI. Multi-scale membrane reactor (MR) modeling and simulation for the water gas shift reaction. Chemical Engineering and Processing-Process Intensification 2018;133:245–62.

[22] Karagöz S, Tsotsis TT, Manousiouthakis VI. Multi-scale modeling and simulation of a novel membrane reactor (MR)/adsorptive reactor (AR) process. Chemical Engineering and Processing - Process Intensification 2019;137:148–58.

[24] Jakobsen HA. Chemical reactor modeling. Multiphase reactive flows. Berlin, Germany: Springer-Verlag; 2008.

[25] Bukur DB, Lang X, Nowicki L. Comparative study of an iron Fischer-Tropsch catalyst performance in stirred tank slurry and fixed-bed reactors. Ind Eng Chem Res 2005;44(16):6038–44.

[26] Froment GF. Fixed bed catalytic reactors. Technological and fundamental design aspects. Chem Ing Tech 1974;46(9):374–86.

[27] Paterson WR, Carberry JJ. Fixed bed catalytic reactor modelling: the heat transfer problem. Chem Eng Sci 1983;38(1):175–80.

[28] Lim JY, Dennis JS. Modeling reaction and diffusion in a spherical catalyst pellet using multicomponent flux models. Ind Eng Chem Res 2012;51(49):15901–11.

[29] Rout KR, Jakobsen HA. A numerical study of fixed bed reactor modelling for steam methane reforming process. Can J Chem Eng 2015;93(7):1222–38.

[30] Keiski RL, Salmi T, Pohjola VJ. Development and verification of a simulation model for a non-isothermal water-gas shift reactor. Chem Eng J 1992;48(1):17–29.

[31] Lund CR. Microkinetics of water-gas shift over sulfided Mo/Al2O3 catalysts. Ind Eng Chem Res 1996;35(8):2531–8.